SPACE ROBOTS

Locomotion as manipulation with ReachBot

Tony G. Chen[1]*, Stephanie Newdick[2], Julia Di[1], Carlo Bosio[1,3], Nitin Ongole[2], Mathieu Lapôtre[4], Marco Pavone[2], Mark R. Cutkosky[1]

Caves and lava tubes on the Moon and Mars are sites of geological and astrobiological interest but consist of terrain that is inaccessible with traditional robot locomotion. To support the exploration of these sites, we present ReachBot, a robot that uses extendable booms as appendages to manipulate itself with respect to irregular rock surfaces. The booms terminate in grippers equipped with microspines and provide ReachBot with a large workspace, allowing it to achieve force closure in enclosed spaces, such as the walls of a lava tube. To propel ReachBot, we present a contact-before-motion planner for nongaited legged locomotion that uses internal force control, similar to a multifingered hand, to keep its long, slender booms in tension. Motion planning also depends on finding and executing secure grips on rock features. We used a Monte Carlo simulation to inform gripper design and predict grasp strength and variability. In addition, we used a two-step perception system to identify possible grasp locations. To validate our approach and mechanisms under realistic conditions, we deployed a single ReachBot arm and gripper in a lava tube in the Mojave Desert. The field test confirmed that ReachBot will find many targets for secure grasps with the proposed kinematic design.

INTRODUCTION

Cliffs, caves, and lava tubes on the Moon and Mars have been identified as locations of intense geological and astrobiological interest. Because of their insulating and shielding properties, these caverns provide relatively stable conditions that may promote mineral precipitation and microbial growth (*1*). On Mars, these ancient subsurface environments are nearly unchanged from when the martian surface was potentially habitable while life on Earth was already evolving (*2*–*4*). In addition, sheltered cavern environments could provide sites for future human habitation (*5*). There is therefore a growing interest in exploring cave-like features that have so far only been examined via orbiter-based remote sensing. Such planetary operations require robots capable of mobility and manipulation in a variety of terrains, particularly rocky terrain and vertical or overhanging surfaces where anchor points may be sparse. NASA's interest in these sites motivates robots that combine sparse-anchored mobility with high-wrench (force and moment) manipulation. However, there is a key technology gap in existing solutions: Small robots typically have a small reach and limited wrench capability. Conversely, large robots, particularly those that use articulated serial links, are hampered by high mass and complexity that scale poorly with increased reach.

ReachBot is a robot concept that locomotes by grasping rock features with multiple appendages, traversing environments that require climbing even when anchor points are sparse (Fig. 1). Using lightweight, extendable booms as appendages, ReachBot achieves a form factor that resembles a harvestman arachnid (Opiliones) (*6*): a small body with very long limbs. Extendable booms have been developed for space applications such as antenna structures (*7*–*9*) because they are light and compact when rolled up but are strong—especially in tension—when deployed and capable of extending many times the span of the robot body. For ReachBot, the tips of the booms are equipped with pivoting wrists and grippers that use arrays of microspines to grasp rocky surfaces. As we discuss in the following sections, this arrangement allows ReachBot to move by manipulating its body with respect to the terrain.

Locomotion as manipulation provides access to the floor, walls, and ceilings of caves or lava tubes. To increase scientific value, robotic investigation of these systems should include subsurface stratigraphy of the walls, which may reveal a great deal about the geologic history of the planetary body (*10*). More broadly, vertical outcrops (whether in caves or along cliffs) offer a unique opportunity to read the geologic record in a spatially continuous fashion but can only be accessed by climbing. These interesting geological features can also contain large crevasses and loose rubble piles that make them difficult for traditional robots to navigate. Existing legged and climbing robots could access some sites of interest, but the lengths of their limbs restrict them to movement along one surface, neglecting the advantage offered by terrain features on the surrounding walls of a cave or lava tube. Conversely, a robot that manipulates itself with extendable booms can leverage anchor points in all directions to bypass obstacles and access vertical outcrops, as well as assume a wide variety of possible configurations, bracing stances, and force application options.

In previous publications, we introduced the ReachBot concept and discussed planar motion planning and control (*11*–*14*). Here, we extend the analysis and motion planning to fully three-dimensional (3D) scenarios and report on field tests of ReachBot technology to pave the way for full-scale ReachBot deployment.

Although locomotion via extending booms is particular to ReachBot, the kinematics and dynamics share similarities to some other established areas of work. The model used for motion planning and control adapts concepts from legged locomotion and from manipulation with multifingered hands, including the formation of a grasp matrix and the consideration of internal and external grasp forces and force closure (*15*–*18*). We used a decoupled motion planning strategy that combines discrete footstep planning with continuous trajectory optimization. Similar strategies have been successful for legged, climbing, and brachiating robots (*19*–*23*), but our combination of a large workspace and potentially sparse anchor points requires a more versatile motion plan that does not rely on a predefined gait. In addition, we assumed that

[1]Department of Mechanical Engineering, Stanford University, Stanford, CA 94305, USA. [2]Department of Aeronautics and Astronautics, Stanford University, Stanford, CA 94305, USA. [3]Department of Mechanical Engineering, University of California, Berkeley, CA 94720, USA. [4]Department of Earth and Planetary Sciences, Stanford University, Stanford, CA 94305, USA.
*Corresponding author. Email: agchen@stanford.edu

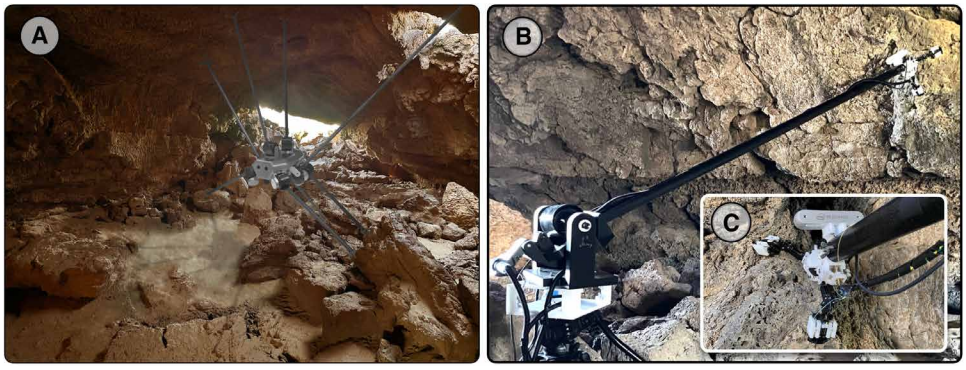

Fig. 1. ReachBot exploring an analog martian lava tube. (**A**) A rendering of a full ReachBot configuration overlaid on our field test site in the Lavic Lake volcanic field in the Mojave Desert. (**B**) The single-boom prototype in the same lava tube to demonstrate deployer, perception system, and microspine gripper, which can be seen grasping from another perspective in (**C**).

model of a general three-finger gripper equipped with spines on a convex rock surface used to compute probabilistic force limit surfaces for grasp planning; a lightweight underactuated gripper specialized for secure grasps on irregular convex surfaces; a perception pipeline that identifies graspable sites from a distance; and empirical field data to support the grasp modeling, grasp site identification, and gripper design. The tests were conducted in a lava tube in the Mojave Desert as a proxy for lava tubes on Mars.

ReachBot moves slowly enough that it does not have inertial swinging dynamics. In particular, we looked to contact-before-motion planners, which offer solutions for robots in terrain that require careful footstep planning (*24*, *25*). ReachBot requires a relatively high effort for each footstep: It must target a site, extend a boom, grasp, and tension the boom. Grasp failures can also degrade the gripper spines and send large transient forces into the robot structure. Accordingly, we sought to minimize grasp failures via risk-aware motion planning, requiring a model of grasp strength. Last, ReachBot also shares similarities with cable-based robots (*26*–*28*), including some cable-based designs proposed for planetary exploration or construction activities (*29*–*31*). Like cables, the booms exert forces primarily along their long axes, and similar issues arise with respect to computing the stability of a stance. Unlike cables, however, booms can be steered toward targets.

Grasping or climbing rocky surfaces with spines has been addressed in various publications, including some that address space applications (*22*, *32*–*37*). The analysis of collections of spines has also been addressed in detail (*33*, *38*–*40*). We drew on this work for the design and analysis of ReachBot's grippers. ReachBot targets convex features with a radius of curvature approximately on the scale of its grippers. This choice reduces the density of targets but results in grasps with a high ratio of pull-off to grasp force. It also requires ReachBot to identify such features in the surrounding terrain.

Our approach to grasp site identification builds on extensive work on perceiving outdoor terrain for legged and climbing robots. This includes offline methods of prescanning a terrain map (*41*, *42*) and online methods that continuously construct and replan on the basis of onboard sensors (*43*, *44*). Because ReachBot must be able to navigate previously unknown caves, onboard sensing is crucial for identifying grasp sites for the planner. Existing microspine-based climbing robots have a comparatively small workspace, so their perception systems can construct detailed surface scans to enable grasp site prediction (*22*). Because ReachBot has a large workspace, we present a two-stage (far and near) vision-based perception strategy to identify rock features and estimate their ability to provide a strong grasp.

We present field tests with a robot that locomotes by manipulating itself in caves and similar terrain. The technical contributions include a 3D simulation and motion planner for ReachBot, identifying gaps in existing work on locomotion in cave-like environments; a kinematic

RESULTS

ReachBot model, control, and motion planning

The architecture for ReachBot used throughout this paper was developed as part of a system design trade study for a mission to a martian lava tube (*13*). This configuration of ReachBot has eight extendable booms—three on either side and two overhead—each with separate pan, tilt, and prismatic actuated joints. The range of motion of an example boom is shown in Fig. 2A. The gripper is mounted on a ball joint wrist with a single degree of actuation for grasping and releasing at the end of each boom.

ReachBot's long, slender booms are susceptible to buckling from compression or bending loads. We can respect their limitations by using concepts from multifingered dexterous manipulation, in particular force closure and internal force control. In dexterous manipulation, fingers apply unisense contact forces to manipulate an object (*15*, *16*, *45*). ReachBot moves analogously to a manipulated object. In place of fingers that push, ReachBot has booms that pull. By ensuring that the booms are always in tension, we leverage the tensile strength of the booms and maintain the stiffness of the entire structure, analogous to a bicycle wheel with tensioned spokes.

ReachBot executes two types of continuous movement that mirror manipulation with a multifingered hand. In body movement ("in-grasp manipulation"), all grippers are attached to the environment, and in end-effector movement ("finger gaiting" or "re-grasp manipulation"), a gripper detaches and moves to a new grasp point. The free-body diagrams in Fig. 2 (B and C) represent the dynamics of ReachBot's body and a detached gripper under the assumption that the distributed mass of each boom is small enough that we can approximate the inertial dynamics using a lumped parameter model consisting of the masses of the body and the grippers. We assume that the attached grippers do not move from their anchor points, so the control inputs shown in Fig. 2B apply a wrench directly to the surroundings. Although the attached grippers support themselves, ReachBot must support any detached grippers. In general, we decouple body movement and end-effector movement as two modes of locomotion with distinct governing dynamics.

During both types of movement, we define a Jacobian, **J**, that relates joint velocities to body linear and angular velocities. We can apply a wrench on the robot body using the relationship

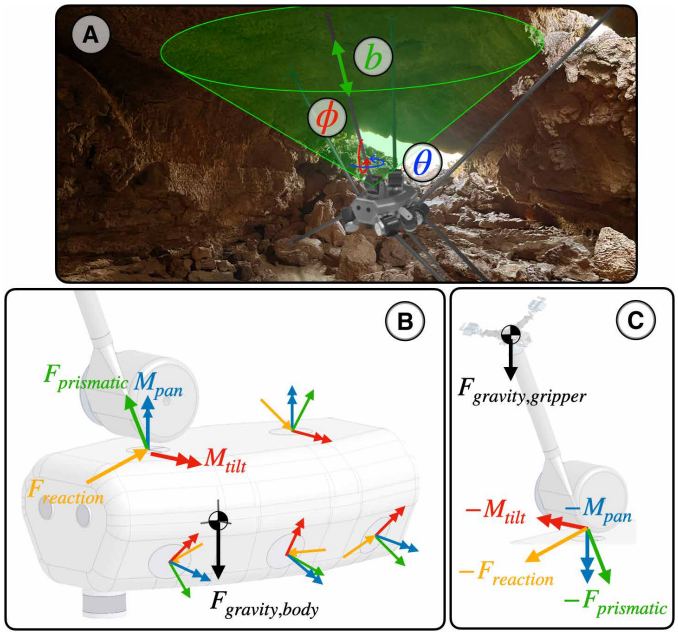

Fig. 2. Visualization of ReachBot's kinematic workspace. (**A**) Each shoulder joint has a pan, θ, and tilt, ϕ, range of motion in addition to a prismatic boom with extension *b*. The model treats boom deployers as points, with their mass incorporated into the mass of the robot body. A free-body diagram for ReachBot's body (**B**) includes the actuated pan moment $\boldsymbol{M}_{\text{pan}}$, tilt moment $\boldsymbol{M}_{\text{tilt}}$, and prismatic force $\boldsymbol{F}_{\text{prismatic}}$ along the boom, as well as a reaction force $\boldsymbol{F}_{\text{reaction}}$ in the plane perpendicular to $\boldsymbol{F}_{\text{prismatic}}$, at each shoulder joint. There is no moment about the boom because of the free wrist. Gravity ($\boldsymbol{F}_{\text{gravity body}} = m_{\text{body}}G$) acts at the center of mass. When a gripper is attached, it supports its own weight, but when detached, the shoulder joint must support it. The free-body diagram for an unattached gripper (**C**) includes interaction forces at the shoulder joint and gravity ($\boldsymbol{F}_{\text{gravity gripper}} = m_{\text{gripper}}G$).

$$\mathbf{W} = -\mathbf{J}^T\boldsymbol{\tau} \tag{1}$$

where $\boldsymbol{W}$ is the applied wrench on the robot body and $\boldsymbol{\tau}$ is a vector of control inputs (one prismatic force and two rotational torques for each shoulder joint). We can solve this equation for $\boldsymbol{\tau}$, but we must apply an additional constraint to maintain tension in the booms. Because there is redundant actuation in the system, $\mathbf{J}$ is not square; therefore, we define

$$\hat{\boldsymbol{\tau}} = \boldsymbol{\tau} + \mathbf{C}\mathcal{N}(\mathbf{J}^T) \tag{2}$$

where $\mathcal{N}(\mathbf{J}^T)$ is the null space of $\mathbf{J}^T$ and $\mathbf{C}$ is a vector of dimension ($\mathcal{N}(\mathbf{J}^T)$) scalars. We use linear optimization to find a solution $\mathbf{C}$ to constrain all prismatic forces to be in tension and minimize control effort. The resulting torque, $\hat{\boldsymbol{\tau}}$, is applied to stabilization, control, or trajectory tracking.

Motion planning for ReachBot requires a combination of discrete footstep planning and continuous trajectory optimization. To take advantage of ReachBot's large workspace and to accommodate the highly irregular terrain, we introduce a decoupled contact-before-motion plan wherein ReachBot uses discrete optimization to generate a footstep plan and then uses waypoint planning jointly with sequential convex programming (SCP) to plan a sequence of continuous body and end-effector trajectories that carry out the footstep plan. The details of the discrete optimization are as per (*14*) but extended to three dimensions. We constructed the simulated environment shown in Fig. 3 on the basis of anchor point data obtained in the Mojave Desert lava tube.

The result of footstep planning is a sequence of stances (assignments that pair *n* end effectors to anchor points) linked by feasible transition poses with an overall goal of moving the body from a starting position to a goal. A feasible pose is one where the robot's configuration is not in collision with itself or with the environment and can hold itself statically within motor torque limits. We assume a transition between 8-stances is feasible if there exists a pose that is feasible: in the starting 8-stance; in the common 7-stance while holding the free boom at its starting anchor point; in the common 7-stance while holding the free boom at its ending anchor point; and in the goal 8-stance. This assumption is true except in pathological cases (for example, abrupt, large changes in tunnel diameter), which are uncharacteristic of lava tubes. To generate the plan, we constructed a graph wherein each 8-stance is a vertex, and each edge represents a feasible transition between stances. Figure 3B shows a sequence of vertices in the footstep plan, with Fig. 3 (C and D) showing examples of a body movement and end-effector movement phase, respectively, that ReachBot takes during its path from start to finish.

During body movement, ReachBot moves within an 8-stance to prepare for the next stance transition. The footstep path guarantees that each pose at the beginning and end of a required body movement is feasible, but we further require every intermediate pose to be feasible. To this end, we generated a discretized trajectory of feasible poses by sampling locally from a straight-line trajectory, verifying at each point that a combination of forces exists to maintain that pose. We generated control inputs for each waypoint in the trajectory using Eq. 2. We then used this trajectory to warm-start the SCP solver, which minimizes control effort and generates a dynamically feasible trajectory. SCP sequentially approximates the nonconvex body movement problem with the following convex optimization problem

$$\min_{\substack{\mathbf{S}_k,\,\boldsymbol{\tau}_k \\ \forall k \in \{1..\,n_{\text{timestep}}\}}} \sum_{k=1}^{n_{\text{timesteps}}} \left(c(\boldsymbol{\tau}_k) + \lambda_s \,||\, \mathbf{S}_k^{(w)} - \mathbf{S}_k^{(w-1)} \,||\, + \lambda_\tau \,|\, |\, \boldsymbol{\tau}_k^{(w)} - \boldsymbol{\tau}_k^{(w-1)} \,|\, | \right) \tag{3}$$

such that (s.t.) $\mathbf{S}_{k+1} = A(\boldsymbol{S}_k, \boldsymbol{\tau}_k) \quad \forall\, k \in \{1..\,n_{\text{timesteps}} - 1\}$

$$\mathbf{S}_1 = \mathbf{S}_{\text{start}}$$

$$\mathbf{S}_n = \mathbf{S}_{\text{goal}}$$

$$\Theta_{\min} \le \Theta_k \le \Theta_{\max} \quad \forall k \in \{1..\,n_{\text{timesteps}}\}$$

$$\boldsymbol{\tau}_{\min} \le \boldsymbol{\tau}_k \le \boldsymbol{\tau}_{\max} \quad \forall k \in \{1..\,n_{\text{timesteps}}\}$$

where the optimization variables are the state vector

$$\mathbf{S}_k = [X_k, Q_k, P_k, L_k] \tag{4}$$

which defines the body position $\boldsymbol{X} = [x, y, z]$, orientation in quaternions $\boldsymbol{Q} = [q_x, q_y, q_z, q_w]$, linear momentum $\boldsymbol{P} = m_{\text{body}}[\dot{x}, \dot{y}, \dot{z}]$ and angular momentum $\boldsymbol{L} = \mathbf{I}_{\text{body}}[\omega_x, \omega_y, \omega_z]$ at time step *k*, and the control vector

$$\boldsymbol{\tau}_k = \left[\mathbf{F}_{\text{prismatic},k\{i\}}, \mathbf{M}_{\text{pan},k\{i\}}, \mathbf{M}_{\text{tilt},k\{i\}} \quad \forall i \in \{1..\,n_{\text{booms}}\} \right] \tag{5}$$

that defines the prismatic force, pan moment, and tilt moment applied to boom *i* at time step *k*. The control inputs $\boldsymbol{\tau}_k$ are bounded

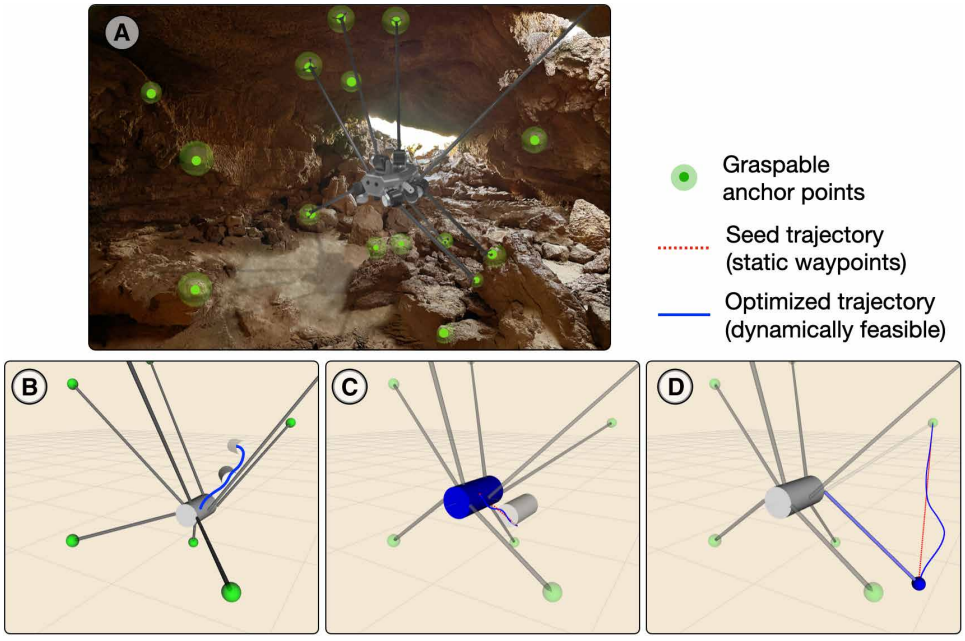

Fig. 3. Motion planning simulation based on a lava tube. (**A**) A rendering of ReachBot in a lava tube near Mojave, CA with graspable anchor points identified with green highlights. (**B**) A sequence of body positions corresponding to vertices in the footstep plan graph. (**C**) A body motion during which all eight grippers remain attached. (**D**) An end-effector motion in which a gripper is detached and reattached at a new location. In each continuous phase, the seed trajectory (sequence of static waypoints) is shown as a red dotted line. The dynamically feasible optimized trajectory is shown as a blue solid curve.

by motor constraints based on hardware limitations. Similarly, joint positions

$$\Theta_k = \left[\, b_{\text{prismatic},k\{i\}}, \theta_{\text{pan},k\{i\}}, \phi_{\text{tilt},k\{i\}} \quad \forall i \in \{1..n_{\text{booms}}\} \,\right] \qquad (6)$$

are bounded by kinematic constraints that limit the length of the boom, pan angle, and tilt angle. We use $(\boldsymbol{S}_k)^{(w)}$ and $(\boldsymbol{\tau}_k)^{(w)}$ to denote the value of $(\boldsymbol{S}_k)$ and $(\boldsymbol{\tau}_k)$ at SCP iteration w; where not explicitly noted, all variables and derived quantities correspond to SCP iteration w.

To minimize control effort, we minimize $c(\boldsymbol{\tau}_k)$, a weighted metric of forces and moments, at all time steps. In particular, the weight of moments in this objective function is scaled with ReachBot's characteristic length, in this case the length of the body. For simplicity, we let $c(\boldsymbol{\tau}_k) = ||\boldsymbol{\tau}_k||$ in this work. In each iteration of the SCP, we penalize divergence from the local convexification using trust parameters for the state λ_s and control λ_τ.

The function A represents ReachBot's dynamics linearized around the previous SCP iteration. Because the seed trajectory $(\boldsymbol{S}^{(0)}, \boldsymbol{\tau}^{(0)})$ is constructed from a string of static intermediate poses, this constraint is necessary to ensure the dynamic feasibility of the final trajectory. Last, to preserve the feasibility of the high-level footstep plan, we require each body and end-effector movement segment to start and end at the state determined by the footstep planner. This is accomplished by constraining $\boldsymbol{S}_{\text{start}}$ and $\boldsymbol{S}_{\text{goal}}$. An example trajectory of body movement is shown in Fig. 3C.

We use a similar technique for free end-effector movement by warm-starting SCP with a locally sampled collision-free straight-line gripper trajectory between anchor points. The optimization is nearly identical to that for body movement but with an external wrench term imparted by the cantilevered boom and end effector included in the dynamics. An example end-effector trajectory is shown in Fig. 3D.

ReachBot's locomotion is contingent on reliable grasps, so a robust motion plan must incorporate knowledge of grasp strength and variability. It is therefore essential to have an accurate model to predict the force limit surface of each anchor point. In addition, we seek to expand ReachBot's accessible terrain by designing a gripper that can withstand large pulling forces and conform to many different rock geometries with a lightweight design. Last, our planner relies on knowledge of anchor point locations beforehand (Fig. 3A), requiring a perception system to aid in grasp site identification. In the following sections, we present solutions to each of these challenges to support ReachBot's locomotion in realistic environments.

Gripper modeling and grasp prediction through limit surfaces

To plan a trajectory through a rocky cave, one must estimate the reliability of possible grasp points. As part of this process, we need to estimate the maximum pull force that a boom and gripper can exert while grasping a rock feature. As noted in previous work (*38*–*40*), grasping rock surfaces with microspines is inherently stochastic but can be modeled with a defined mean and SD. In contrast to some previous applications involving arrays of microspines (*22*, *38*, *46*, *47*), we do not assume that the surface is nearly flat at the length scale of the gripper; instead, we seek rounded features that the gripper can partially enclose. This condition increases the pull force for a given number of spines.

To estimate the pull force limit distribution, we perform an analysis wherein we assume that the gripper is grasping a rounded rock feature that can be approximated as a spherical patch with radius r. The gripper is symmetric, with three fingers, each having two links of length ℓ (Fig. 4). For a locally spherical surface, links of equal length provide the tightest fit to the surface. A pulling force, $\boldsymbol{F}_{\text{pull}}$, is applied to the wrist joint with a direction defined by the two angles β and ϕ. When the gripper is loaded, the wrist joint will be a small distance, x, away from the surface. We now consider a single spine that is part of a small array of spines at one of the fingertips. As in (*38*–*40*), the spine tips do not penetrate the rock surface and are subject to Coulomb friction. Thus, for each spine, the ability to sustain loads $\boldsymbol{F}_{\text{ti}}$ and $\boldsymbol{F}_{\text{ci}}$ in the local tangential directions is a function of the normal force, $\boldsymbol{F}_{\text{ni}}$, and the angle of inclination at which it makes contact. The overall angle is a function of where the spine rests on an asperity (illustrated as a small hemispherical bump in Fig. 4A), parameterized by ψ_i, and by the local surface normal in the vicinity of the asperity, which is parameterized by α_i. The angle α_i is a function of how much the gripper encloses the rocky feature. For a flat surface, $\alpha = 0$; if $r < \ell$, $\alpha \to \pi/4$. The normal force, $\boldsymbol{F}_{\text{ni}}$, is a function of both the applied load to the fingertip and the internal grasp force, $\boldsymbol{F}_{\text{pi}}$, which we can control. Computing the force balance

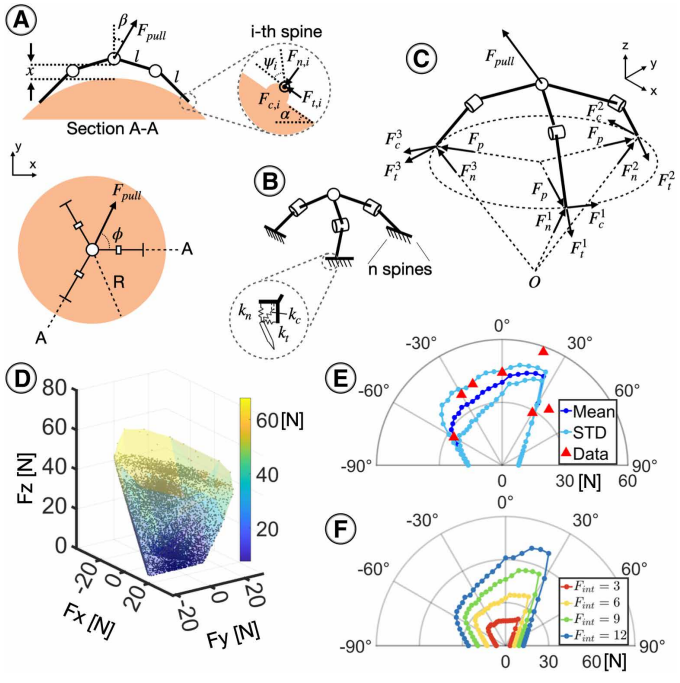

Fig. 4. Grasp model and analysis. (**A**) Geometric parameters for three-finger grasp model. (**B**) Free body diagram and contact forces. (**C**) Compliant spine-asperity contact. (**D**) A 3D limit surface generated from a Monte Carlo simulation with 10,000 samples using parameters derived during the field test; force components are with respect to (*x*, *y*, and *z*) coordinates in (B), in a frame centered at the wrist. (**E**) Cross-sectional polar plot of the magnitude of applied pull force, $\boldsymbol{F}_{\text{pull}}$, using parameters from field test, with ($-90^\circ \leq \beta \leq 90^\circ$), where β is the pull angle, and assuming 20 spines engaged (25%). Slight asymmetry in α arises from asymmetry in the rock. Straight sides correspond to failure associated with a finger lifting off. Red triangles mark field test results. Additional details are provided in Supplementary Methods. (**F**) Cross-sectional polar plot showing the dependence of $\boldsymbol{F}_{\text{pull}}$ on grasp force, $\boldsymbol{F}_{\text{int}}$.

and assuming Coulomb friction, we have the no-slip condition for a spine

$$\frac{\sqrt{\left(\mathbf{F}_{t,i}\cos\psi_i - \mathbf{F}_{n,i}\sin\psi_i + \mathbf{F}_{p,i}\cos(\alpha+\psi_i)\right)^2 + (\mathbf{F}_{c,i})^2}}{\mathbf{F}_{t,i}\sin\psi_i + \mathbf{F}_{n,i}\cos\psi_i + \mathbf{F}_{p,i}\sin(\alpha+\psi_i)} \leq \mu \qquad (7)$$

The derivation of this expression can be found in Supplementary Methods. We note that the no-slip condition depends not only on the asperity distribution but also on α, which increases as the surface becomes increasingly convex. This dependency, along with the grasp force balance equations described below, accounts for the ability to provide larger pull-off forces for a given grasp force when grasping convex features. A similar relationship has been noted for perching air vehicles that use claws to grasp branches or tree trunks (*48*).

For an array of spines, there will be a distribution of asperities, leading to a distribution of angles with corresponding variations in the maximum tangential forces. If we assume a distribution of angles, ψ_i, we can compute the overall contact force limits for an array of spines at each fingertip, following a procedure similar to that in (*33*, *39*, *40*).

Whether the array of spines at each fingertip slips or holds also depends on the overall force balance for the hand. The hand has a ball joint at the wrist, so no torques are transmitted. We construct a grasp matrix, assuming that the spine array at each fingertip is compact enough to be treated kinematically as a point contact. This is further justified by how the spines are supported in compliant suspensions so the spine array does not produce substantial bending moments about the contact. Given an assumed external force $\boldsymbol{F}_{\text{pull}}$ and known geometry, we have nine quantities to solve for, corresponding to the normal and tangential force components at each contact. Force equilibrium provides six equations. In addition, we have three kinematic equations stemming from the condition that spines do not penetrate and should not lift off from the rock surface. This rigid body condition can be converted into equations on the forces using the known suspension stiffnesses (k_n, k_t, k_c) at each spine. The result is an invertible system

$$\mathbf{AF} = \mathbf{B} \qquad (8)$$

where **A** is a 9×9 compliant grasp matrix that maps contact forces to resultant forces at the wrist, **F** is the vector of contact forces to be solved, and **B** is a nine-element vector containing terms with $\boldsymbol{F}_{\text{pull}}$ and the pull angles, β and ϕ. Details of the derivation are provided in Supplementary Methods.

Equations 7 and 8 can be computed for a given grasp geometry and gripper, summing the contributions for arrays of spines and assuming a distribution of asperities, parameterized by ψ_i. We perform a Monte Carlo simulation by running this computation over many samples of asperity angles to approximate the distribution of the maximum magnitude of the pulling force and then sweeping over the direction of the pulling force (β, ϕ) to generate a grasp limit surface. Details of the Monte Carlo simulation are provided in Supplementary Methods. A sample limit surface is shown in Fig. 4 using the following parameter values: $n_{\text{spines}} = 20$, $\alpha_1 = 1.22$ rad, $\alpha_2 = 0.52$ rad, $\alpha_3 = 0.70$ rad, $\mu = 0.39$, $r = 11.6$ cm, $x = 4.5$ cm, $F_{\text{int}} = 6$ N, $F_{\max} = 12$ N (maximum tangential force for a single spine to prevent permanent bending), $k_n = 15\ \text{N}\cdot\text{m}^{-1}$, $k_t = 3 \times 10^6\ \text{N}\cdot\text{m}^{-1}$, $k_c = 1\ \text{N}\cdot\text{m}^{-1}$, $n_{\text{iterations}} = 200$. These values correspond to our estimates for the field tests on lava rock using data from a lava tube, obtained by the perception system as described in the section on grasping site identification.

The limit surface model is applied during motion planning to evaluate potential grasp sites on the basis of rock geometry and expected pulling directions. The model is also useful for comparing limit surfaces of different gripper designs for a given set of grasp geometries, thus aiding in selecting a gripper design for a specific application.

Gripper design

The primary design requirements for the grippers include low weight, high conformability to rock features, and large direction-dependent maximum pullout force as quantified by the limit surface. The evaluated force directions should correspond to the anticipated range of boom pulling directions. The need to minimize weight is driven by two considerations: A heavier gripper produces higher bending loads that may cause the booms to buckle and increases the torque required by the shoulder actuators to steer the boom.

To meet the requirements, we designed and tested an underactuated, tendon-driven gripper with microspines (Fig. 5A). The gripper has three fingers, each with two phalanges. To save weight, the entire gripper is actuated by a single motor (Fig. 5B). As in some other underactuated grippers (*47*, *49*), the main tensile loads are borne by the tendons and not the joints.

Two sets of tendons are used to close and open the fingers (Fig. 5, D and E). The tendons are driven by a motor with a non-backdrivable transmission and high gear ratio, which permits moderate grasp forces (≈7.5 N on each finger), albeit with slow operation (≈20 s to close

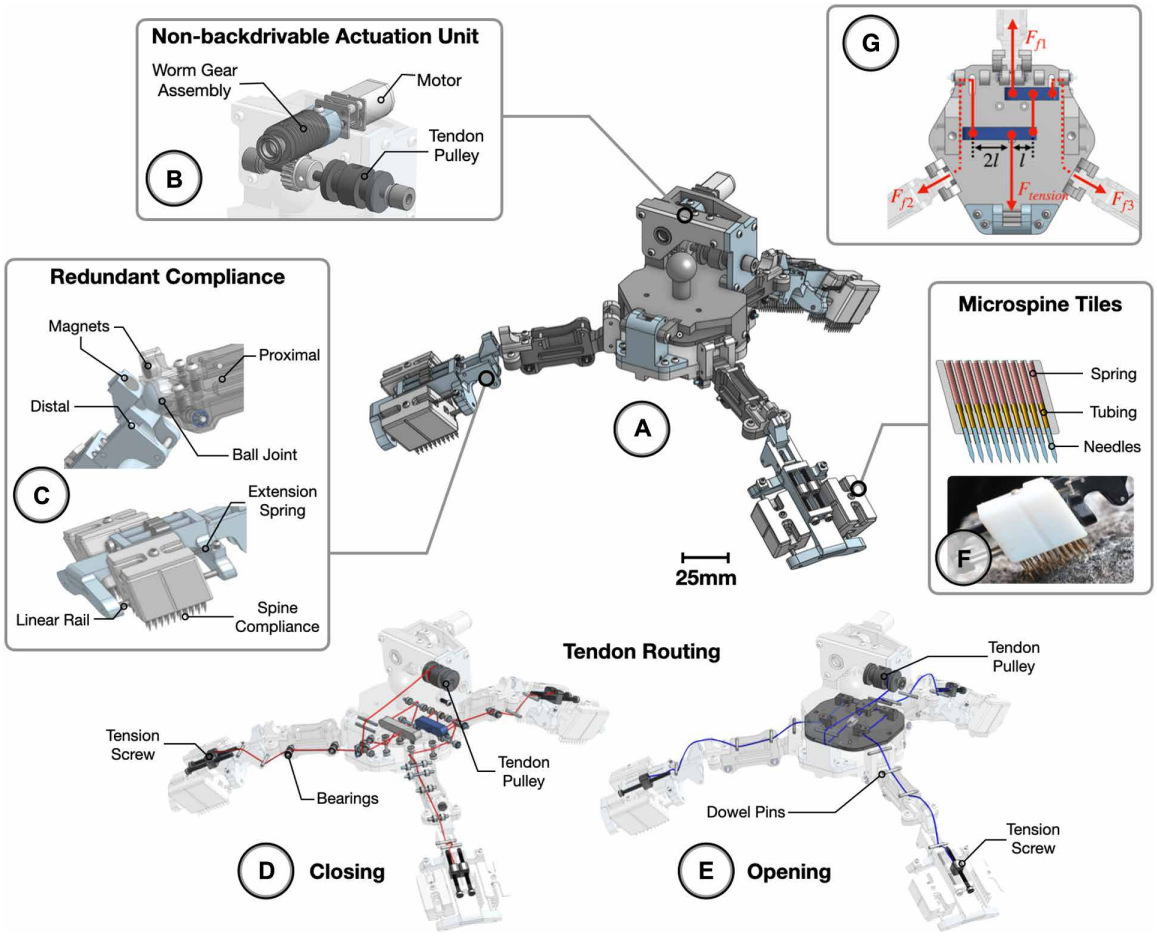

Fig. 5. Mechanical gripper design. (**A**) Opening and closing tendons are driven by a single gearmotor and drum (**B**). Proximal/distal phalanges are connected by ball joints, with permanent magnets to hold them in place when the hand is open (**C**). The opening and closing tendons, respectively, are illustrated in (**D**) and (**E**). Linearly constrained spines (**F**) are arranged in compact arrays on carriages that float with respect to the fingertips. The closing tendons converge into a single tendon through a three-way whiffletree load sharing mechanism (**G**). Additional details are provided in Supplementary Methods.

the hand from a fully opened configuration). The closing and opening tendons are wrapped around a drum that is fixed to a shaft with a worm gear assembly (Fig. 5B). The two primary tendons are wrapped around the drum separately, one clockwise and one counterclockwise for opening and closing, respectively. As in many underactuated hands, a differential mechanism divides the tendon forces among the fingers for closing (*50*). In the present case, we used a three-way whiffletree, illustrated in Fig. 5G.

A known issue with compliant underactuated hands is that one wants the proximal joints to start closing before the distal joints to achieve a large "acquisition region" (*50*, *51*). In hands that use torsion springs or other elastic elements, this requirement can lead to either floppy proximal joints in the relaxed state or stiff distal joints, which increases the effort required for grasping. Solutions can include exploiting nonlinearities in the joint stiffness (*52*). Here, we used pairs of permanent magnets at the medial joints (Fig. 5C) that hold the fingers precisely in the fully extended position until tension in the closing tendon causes the joint torque to exceed a threshold determined by the strength of the magnetic force, by which time the proximal joints have already started to flex. With this provision, the stiffnesses of the joints can be adjusted to prevent the distal phalanges from curling inward prematurely when grasping small convex features. Similar uses of magnets to achieve a nonlinear stiffness in underactuated hands can be found in (*53*, *54*).

Rock surfaces, especially lava rocks, are highly irregular at both macroscopic and microscopic scales. Therefore, compliance is built into the hand at multiple length scales. At the microscopic scale (<100 μm), asperity size determines the required spine tip radius. In this regard, the rock samples in a lava tube are similar to other rocks climbed by robots with spines (*22*, *32*, *47*), and the spine tip radius (≈10 μm) is comparable. At a slightly larger scale, surface waviness determines how much linear travel the spines should have to ensure that enough spines on each tile will contact the surface. We assumed ≈25% asperity engagement in the analysis in the previous section. A surface scan of the rock in Supplementary Methods revealed that there is substantial waviness at the approximately 1-cm scale. To accommodate this waviness, the spines have 10-mm linear travel. In practice, we have observed empirically that at least 25% of the spines do actively engage. The third relevant scale of surface waviness is at the length scale of the hand. We rely on the existence of rounded features, and we designed the hand to be able to conform to these features so that all the fingertips make contact. This topic is addressed further in the reachability analysis in the next section and in Fig. 6.

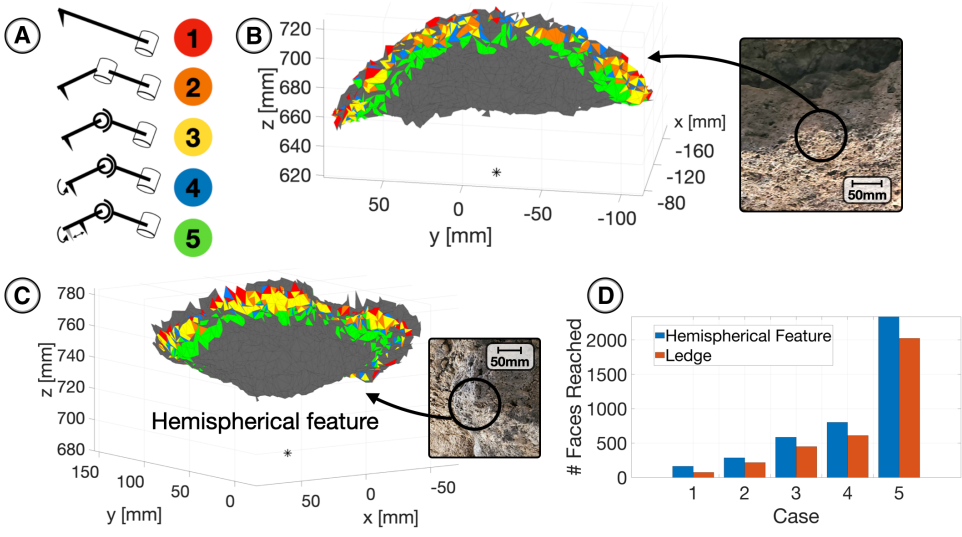

Fig. 6. Reachability analysis of different gripper configurations. (**A**) Representative lava rocks presenting hemispherical (**B**) and ledge (**C**) surface patches scanned and meshed at ≈0.1-mm resolution (insets show actual surface). Red: In the first case, there is one phalange with the spine fixed at the end. Orange: In the second case, there are two phalanges connected with a revolute joint. Yellow: In the third case, there are two phalanges connected with a ball joint. Blue: The fourth case is the same as the third case, with the spine able to rotate with respect to the distal phalange. Green: The fifth case is the same as the fourth case, with the spine having up to 10-mm tangential and normal linear travel with respect to distal phalange. On meshed surfaces, each colored region depicts the additional graspable area with respect to the previous case. (**D**) Comparison of reachable areas for the different cases for each surface.

At the tip of each finger is a pair of compliantly supporting microspine arrays (Fig. 5C). As described in (*33*, *46*), arrays of linearly constrained spines provide high packing efficiency for maximum shear force per unit area. To provide more compliance and conformability than in these earlier designs, the arrays slide semi-independently on rods, with a compliant coupling. Each floating carriage is connected to the distal structure through one rod, thus allowing for both linear compliance and torsional compliance with respect to the finger. These suspension elements, along with a small amount of compliance for each spine (Fig. 5F), provide load sharing so that the first few spines to make contact with asperities do not take most of the load and fail prematurely. A similar floating tile design is seen in a climbing robot (*34*).

As noted in the previous section, we exploit rounded rock features to increase the ratio of pull-off force to grasp force. Features can exhibit approximately spherical or cylindrical geometries, for knobs or ledges, at the length scale of the hand. To accommodate both of these geometries, the fingers have ball joints that allow bending and twisting. With this flexibility, the gripper can passively assume either an approximately symmetric three-fingered grasp or an opposed grasp, with two fingers opposite the third finger, as it is closed and loaded.

Some questions not yet addressed are how many degrees of freedom the gripper fingers require and how many phalanges they should have. To address this question, we conducted numerical studies with typical lava rocks for a single finger, as illustrated in Fig. 6. For simplicity, there is only one spine at the end of the finger; we assume that there is enough compliance in the spine tiles and spines that we can obtain roughly 25% spine contact for the range locations and angles simulated for a single spine. Even so, the search space is large, and an exhaustive search is prohibitive. However, for one-phalange and two-phalange designs with different joint types, we can examine the ability to conform to rock surfaces with typical (partial) spherical and cylindrical shapes. For effective grasping, each spine will need to meet the surface at a range of angles between 10° and 30° from the surface normal. Figure 6 illustrates five cases with sequentially increasing mobility. In the first case, there is one rigid phalange with a revolute joint at the base. In the second case, two phalanges have a revolute joint between them. In the third case, there are two phalanges with a spherical joint in between. The fourth case is the same as the third case with an additional rotation degree of freedom at the spine. The fifth case is the same as the fourth case with additional shear compliance of the spine. Each shaded region highlights the additional surface area that can be grasped in comparison with the previous case. As illustrated in Fig. 6D, the fifth case represents a substantial improvement over the previous cases, which is why it was incorporated into the gripper design.

The prototype gripper presented in this paper reflects the design requirements for grasping rough convex rock surfaces with high reliability. Force tests were limited to avoid breaking the 3D-printed plastic parts. We expect the trend of increasing $\boldsymbol{F}_{\text{pull}}$ with $\boldsymbol{F}_{\text{int}}$ seen in Fig. 4F to scale to larger loads, limited by the chosen motor, tendons, finger components, and surface asperity strength.

Grasping site identification and selection

Grasp strength is strongly dependent on surface profile, but the repositioning, detaching, and deployment of a gripper toward a new site can be a time-intensive maneuver limited mainly by the speed of boom steering and deployment. Therefore, it is beneficial for ReachBot to have high confidence in a potential grasp before committing to extending its end effector. Our solution is a two-stage image-based surface scanning process: A cursory scan from the body provides rough indications of suitable grasp sites, such as convex features. It then samples from an extended boom to refine the grasp site evaluation. In this strategy, there are two main geometric parameters that must be determined for the subsequent limit surface analysis.

The first objective is to find suitable convex surfaces. For the present, we approximate these by fitting spheres of radius r onto protruding rocks from a distance. Although there are many methods for spherical approximation, we use the M-estimator SAmple Consensus (MSAC) algorithm for sphere fitting, a variant of RANdom SAmple Consensus (RANSAC). RANSAC is a widely used method for fitting geometric shapes onto data (*55*, *56*), and we chose the MSAC variant for better performance with noise (*57*, *58*). We constrain the output with a window of desired values for ℓ/r, which relates to α as shown in Fig. 7C, with the computation using the same parameter values as the limit surfaces plotted in Fig. 4. This plot also shows that the ratio of pull-off force to grasp force grows rapidly as α and l/r increase from the case of a flat surface ($\alpha = 0$) to a rounded feature and plateau well before the local surface normals at the fingertips become radially

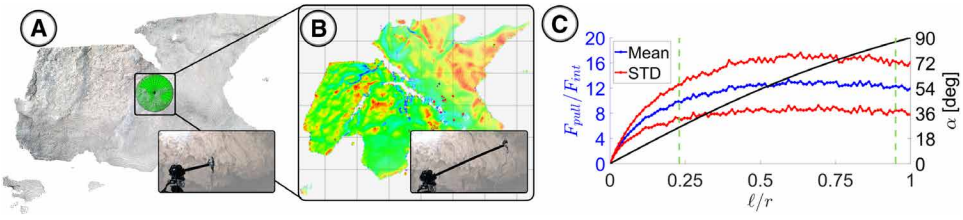

Fig. 7. Two-stage perception and detection of suitable grasp sites. (**A**) From a stowed position away from the rock wall, raw camera depth data were processed to identify a promising region, with roughly spherical features. Inset shows an image of the deployer in a stowed position collecting data from a rock wall. (**B**) The boom is deployed for a closer scan, from which a local α angle heatmap was generated. Red surfaces are nearly flat at the scale of the gripper; green regions correspond to a range of values $\alpha_{min} < \alpha < \alpha_{max}$, where α is the local surface normal in the vicinity of the asperity, that are likely to yield strong grasps. (**C**) Plot for $\beta = 0$, where β is the pull-off angle of the computed ratio of pull-off force to grasp force for different ℓ/r values, where ℓ/r is the ratio of link length to rock radius. The desired range of ℓ/r values is marked (related to α values) with vertical green dashed lines.

opposed. Details of the relationship between ℓ/r and α are provided in Supplementary Methods. Because ReachBot has a large workspace, we assume that we can afford to be selective when determining grasp sites. If multiple nearby grasp sites are available, they are ranked on the basis of computed limit surface models and the preferred loading direction(s), which depend on the stance and desired trajectory of the robot. For field tests reported in the next section, there is a single loading direction corresponding to the fixed angle of the boom. Once a boom is close to a region of interest, a second objective is to determine more precisely the value of α to compute the limit surface and allow for readjustment before committing to a grasp. The α angles are calculated as the angle between the gripper reference axis and the estimated normal vector for the points in the point cloud. ReachBot commits to a grasp if α falls within a range of acceptable values between $\alpha_{min} = 25°$ (below which the pull force drops rapidly for most pulling angles) and $\alpha_{max} = 85°$ (above which there is not substantial improvement in pull force). These bounds were chosen on the basis of when the ratio of pull-off force to grasp force plateaus (Fig. 7C). The upper bound is further dictated by the camera's inability to discern a steep ledge from a potentially discontinuous surface. Mapping α angles spatially can also help categorize the convex surface as roughly hemispherical or as a ledge, which informs the limit surface and subsequent motion planning.

Figure 7 illustrates the main perception pipeline principles used to detect a grasp site. First, from a distance, potential anchoring sites are determined by approximating them as convex surfaces with a radius r, with only promising ℓ/r ratios kept. Figure 7A highlights a convex surface with estimated radius $r = 17$ cm. Once the boom has extended toward an anchoring site, more detailed depth data are gathered to determine the angle α for the limit surface model, as shown in Fig. 7B. The calculated α angles for a successful grasp on this rock were between 55° and 60° for each microspine tile, suggesting that the site is a gently curved hemispherical surface. The two-step perception strategy was also used to compute the r and α values to generate the limit surface plots in Fig. 4 (D to F). The components of the perception system illustrated in Fig. 7 correspond to the field test site.

Deployment in a lava tube

As noted earlier, planetary caves and lava tubes are among the most promising geological and astrobiological targets in the solar system (*59*–*62*). Given that martian lava tubes are of particular interest (*1*, *63*), we decided that a field test of ReachBot technology should be conducted in a reasonable analog on Earth. To this end, tests were conducted in an unnamed lava tube near Pisgah Crater, within the Lavic Lake volcanic field in the Mojave Desert, California (34° 44' 59.0" N116° 22' 03.1" W).

The Lavic Lake volcanic field consists of Quaternary [likely late Pleistocene (*64*)] basaltic pahoehoe and aa lava flows (*65*) and has a long history of serving as a planetary analog (*66*, *67*). The presence of both pahoehoe and aa flow textures ensures that the ReachBot prototype is subjected to a wide range of surface roughnesses, similar to what could be encountered on Mars. The specific lava tube where field testing was conducted was chosen after an initial survey of local lava tubes on the basis on practical considerations, such as entrance size, ease of access, and safety to human operators.

The partial ReachBot prototype in the field test consists of a single boom deployer mounted on a shoulder joint that allowed it to pan and tilt. The gripper, presented in Fig. 5, is mounted at the end of the boom along with an Intel Realsense d455 camera. The entire assembly is mounted on a tripod, representing the body of ReachBot, and is controlled via teleoperation. The overall assembly is shown in Fig. 1B. A fully functional ReachBot will have eight of these shoulder assemblies supporting a central body.

The single-arm prototype was able to target, deploy, and grasp many target sites within the lava tube. One full sequence is shown in movie S1. For the perception system, the field test confirmed the advantages of a two-step perception strategy, starting with a remote scan with the red green blue–depth (RGBD) camera (Fig. 7A). The remote scan, conducted under teleoperation, identified areas that were expected to yield fruitful grasp locations (Fig. 7B). Figure 8 (B to D and E to G) shows grasps on features with approximately spherical (radially symmetric) and cylindrical geometry, respectively. In these images, the boom had been removed for measuring pull-off forces with a Mark-10 (model M4-50 with 0.1-N resolution) force gauge. The gripper is loaded in the direction of the boom. In all cases, the grasps achieved at least 34.2 N (larger forces were not applied to avoid breaking the 3D-printed plastic components of the prototype during field testing).

Additional pull-off tests using only the gripper were subsequently applied by hand using a large rock sample acquired at the testing site. In these tests, the gripper was placed on a surface of the rock and then pulled until the grasp failed, either from part of the 3D-printed structure failing or from the spines breaking or slipping. The maximum force in these tests was recorded, again using the Mark-10 gauge, and the pulling angle was recorded from digital photographs. These results are plotted on the modeled limit surface for the same geometry and gripping parameters in the limit surface in Fig. 4E.

DISCUSSION

We have presented a robot capable of navigating scientifically promising but previously inaccessible areas, such as planetary caves and lava tubes. The work in this paper extends preliminary studies using a simplified planar ReachBot model (*11*, *12*) to a full 3D analysis with a

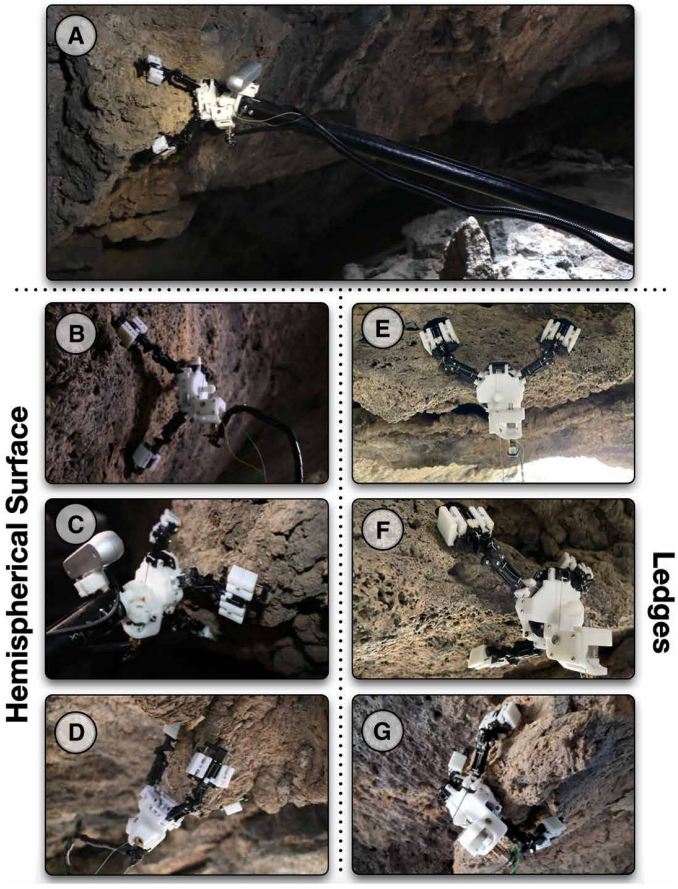

Fig. 8. Field test demonstrations at a lava tube in the Mojave Desert. (**A**) Gripper deployed at end of boom after identifying a target. (**B** to **D**) Locally spherical rock features and (**E** to **G**) locally cylindrical features. In (B) to (G), the boom was removed for pull tests with a force gauge.

realistic consideration of grasp strength and grasp site selection. The results presented here also include field testing because the details of sensing and grasping rock surfaces characteristic of lava tubes are difficult to address purely in simulation. In comparison, many of the motion planning and control considerations can be addressed in simulation once accurate grasp models are available. On the basis of considerations of grasping the rocks in lava tubes, we adopted a strategy of seeking convex features that afford a high ratio of pull-off force to grasp force. To this end, we developed a model of a theoretical three-fingered microspine gripper that can be used to estimate a force limit surface on the basis of different surface geometries and gripper parameters. On the basis of these principles, we prototyped a highly compliant underactuated microspine gripper. For field tests, we also developed a two-step perception system that identifies possible grasp locations, trading density of targets for a high ratio of pull-off to grasp force. Last, we tested a single-arm prototype in a lava tube in the Mojave Desert. During this field test, the ReachBot prototype identified, targeted, and grasped many sites, demonstrating the potential capability of a full ReachBot system while also identifying some real-world challenges for future mission success. There remain many challenges and areas of future work in motion planning, mechanism design, and perception. First, the dynamic model should include the distributed mass of the booms. In addition, the control effort metric $c(\boldsymbol{\tau}_k)$ now penalizes prismatic force and motor torque equally but should balance the relative risk of failure from high prismatic forces (which could cause gripper failure) with the failure from high motor torque (which could cause the boom to buckle).

Second, because of the stochastic nature of spine-surface interactions, grasp failure is an eventuality that must be considered in planning. A robust motion plan must ensure both that the probability of failure is low and that if a grasp does fail, a contingency trajectory exists to stabilize ReachBot with a low likelihood of additional failures. We have identified these challenges in a simplified planar model (*14*) but need to extend them to three dimensions. Numerous improvements to the computational efficiency of the grasp force computation and motion planning are also possible.

Third, to support the force control assumed by ReachBot's motion plan, each boom will need to have force sensing capability. Force sensing will also help to avoid overloading components. In addition, a stronger and more reliable boom deployer will be needed for future prototypes. On the basis of different mission-specific gripper requirements, stronger grippers with metal parts, stronger (or more numerous) spines, and a larger motor can be chosen. A finding from field tests is that it may be desirable to add an actuated roll degree of freedom to better align the gripper with asymmetric features. This addition will increase the distal inertia but is probably worthwhile to increase the density of grasp targets.

Fourth, because ReachBot is a robot with exceptional workspace, its perception system must be designed for its unique form factor. In addition, although the core principles of two-stage sensing were verified, a more flexible shape approximation approach will be investigated. Forthcoming work includes a wider range of geometric feature descriptors, targeted illumination for sensing at different ranges, and inquiry into other long-range sensing beyond the Realsense camera. We will also investigate deep learning approaches for grasp site identification.

Further, a hybrid boom-and-cable design is an interesting possible direction for ReachBot. For example, booms can be used to position and attach anchoring grippers with tensioned cables. Accordingly, one or two booms per robot simplify the articulation of a full system while maintaining a large workspace. Another advantage is that cables could cover even greater distances than extendable booms. A hybrid ReachBot could use a boom to position a gripper while the robot is closer to a desired surface and pay out cables that allow the robot to move much further away than the length of the original boom.

Last, we note that ReachBot's characteristic parameters can be scaled on the basis of the expected environment. For example, boom size relates to gripper size, which relates to tile size and graspable feature size. The scaling chosen for this field test is a good match for the surface characteristics of lava tubes in the Mojave Desert, which are discussed in Supplementary Methods. Accordingly, we may change the entire scale of ReachBot for operation on Mars, the Moon, or other extraterrestrial bodies.

In summary, many extensions are possible. Nevertheless, the work presented in this article provides the basis for the motion planning of a small robot with long arms terminating in grippers that grasp on rocky terrain. Results from the field test confirm the predictions of maximum grasp forces and underscore the importance of identifying and steering toward convex rock features that provide a strong grip. They also highlight a characteristic of grasp planning with ReachBot,

which is that identifying, aiming for, and extending booms involves a higher level of commitment than grasping objects in manufacturing scenarios.

MATERIALS AND METHODS

3D simulation environment

To support our need for a simulation environment with variable-length links and hybrid dynamics, we built a custom physics-based simulation in Python. We used the Rospy package to support visualization using RViz and future hardware integration. We implemented SCP optimization using CVXPY and used standard proportional-integral-derivative control for trajectory tracking. The simulation environment was generated to match our field test site, and constants such as pan and tilt actuator limits were chosen to match our real boom. Parameters used in the simulation are shown in Table 1.

Spine array fabrication

Each microspine used was manufactured from a leather sewing needle with a titanium-nitride finish (Organ Needle HAx130N PD). The sewing needle tip was cut from the stem at a 7-mm length, then inserted into a stainless steel tube (McMaster Carr 8987 K521), and secured in place with superglue (Loctite 401). The stainless steel tube was then inserted into a compression spring (Lee Springs CIM010ZL 05S) with a 3-mm overlap, also secured with superglue (Loctite 401). The spine suspension assembly then was placed into a 3D-printed (Stratasys Objet VeroWhite) spine tile array where the inside lip of the hole holds the edge of the stainless steel tube in place (Fig. 5F).

Gripper fabrication

Most of the gripper components were manufactured through 3D printing using three different printers. The spine tiles were printed with Stratasys Objet VeroWhite for the dimensional accuracy required. The fingers were printed with HP Multi Jet Fusion Nylon 12 PA. The rest of the gripper was printed on a Formlab3+ with Rigid 4k material for rigidity. The connections between parts were accomplished by press-fitting brass screw to expand inserts. The motor (Pololu 1000:1 Micro Metal Gearmotor) underwent a further 30:1 gear reduction through a wormgear assembly (Misumi SUW0.5-R1 and G50B20 + R1) and controlled the loading tendon (Twinline braided Vectran 125) and opening tendon [Power Pro Spectra 18kg (178 N)].

Table 1. Parameters used in ReachBot simulation.

Constants	Joint limits
$G = 3.721\ \text{m s}^{-2}$	$\theta_{min}, \theta_{max} = \pm 180°$
Body length = 0.8 m	$\phi_{min}, \phi_{max} = \pm 90°$
Body diameter = 0.4 m	$b_{min} = 0.2$ m
$m_{body} = 10$ kg	$b_{max} = 10$ m
$m_{gripper} = 1$ kg	$F_{min} = 0$ N
	$F_{max} = 40$ N
	$M_{min}, M_{max} = \pm 10$ N m

Limit surface experimental setup

To validate the limit surface, pull tests were performed with the gripper on volcanic rocks collected from the field test site. A digital force gauge (Mark-10, model M4-50, 0.1-N resolution) was connected to the gripper along a tendon. The angle of the force applied was measured by analyzing photos taken during the experiment. We note that tests to failure typically blunt the spine tips unless something else fails first. Therefore, the probability of each spine finding an asperity gradually diminished as these tests continued. When operating the robot, one would seek to avoid such failures.

Grasp reachability analysis

To analyze reachability, we obtained a triangulated mesh of a scanned rock surface, chose a point slightly above the rock surface to position the base of a simulated finger, and then examined five cases as described in Fig. 6 using Algorithm S2. We sampled each additional degree of freedom at 5° increments and translation in 2-mm increments. We then followed Algorithm S2 to look for rock faces that are reachable by the spine, at which the spine attacked the face at the desired angle (between 10° and 30° from the surface normal) and the finger itself did not collide with the rock.

Perception system field test

The perception field test used an Intel Realsense d455 RGBD camera that was rigidly mounted to the distal end of the boom, colocated with the gripper wrist. The camera provided data from a range of 0.6 to 6 m.

The point cloud was down-sampled using a voxel size $v = 0.5$ cm. To determine regions of interest to investigate, a simple approximation was made to look for spheres of best fit from a distance using MSAC in MATLAB (Algorithm S3). Only rocks with a suitable link length–to–rock radius ratio ℓ/r were kept as potential regions to extend to. For our specific gripper, ℓ was about 60 mm, and there additionally was a palm radius of 30 mm, leading to a full extension of radius 150 mm. A reasonable ℓ/r ratio was 0.35, from a rock with $r = 170$ mm. For the field test, we defined a window $75\ \text{mm} \leq r \leq 200\ \text{mm}$ to quickly filter promising regions of interest.

Once a boom extended to a region, to determine α, the raw depth data stream was processed as a point cloud. The point cloud was down-sampled using the same process as above, and normal vectors were estimated from the local neighborhood of points as defined by the k nearest neighbors, kn. The angle α was calculated as the angle between the normal vector and gripper z axis (Algorithm S4). Limit surfaces can be generated using the three α values and r value of the grasp in the Monte Carlo simulation.

Field testing experimental setup

The deployer was custom built with three different actuators to provide the necessary functionality of a ReachBot shoulder joint. The deploying mechanism (3D-printed, Creality Ender 3 PLA) was a friction-drive wheel powered by a DC motor (Pololu 75:1 Metal Gearmotor). This drive wheel was pressed against the boom coil by compression springs. An additional DC motor (Pololu 75:1 Metal Gearmotor) controlled the elevation of the boom with timing belts and pulleys. The entire assembly was mounted on a turntable (McMaster Carr 6031K16) powered by a servo (Zoskay 35 kg) that controlled the pan angle.

The deployer and gripper were controlled by a single Arduino Mega with manual input from a joystick and serial commands through universal serial bus (USB) from a laptop for the gripper. The pan-angle servo was driven using pulse-width modulation (PWM) signals

from the Arduino Mega. All DC motors were powered by a 12-V power supply, and the servo motor was powered by a separate 6-V power supply.

Statistical tests

For the Monte Carlo simulation, the mean of the data was calculated with the sum of all values divided by the total number of values. The standard derivation of the data was calculated by taking the square root of its variance.

Supplementary Materials

This PDF file includes:

Figs. S1 to S4
Table S1
Algorithm pseudocode S1 to S4

Other Supplementary Material for this manuscript includes the following:

Movie S1
MDAR Reproducibility Checklist

REFERENCES AND NOTES

1. R. J. Léveillé, S. Datta, Lava tubes and basaltic caves as astrobiological targets on earth and mars: A review. *Planet. Space Sci.* **58**, 592–598 (2010).
2. T. C. Onstott, B. L. Ehlmann, H. Sapers, M. Coleman, M. Ivarsson, J. J. Marlow, A. Neubeck, P. Niles, Paleo-rock-hosted life on Earth and the search on Mars: A review and strategy for exploration. *Astrobiology* **19**, 1230–1262 (2019).
3. J. P. Grotzinger, D. Y. Sumner, L. C. Kah, K. Stack, S. Gupta, L. Edgar, D. Rubin, K. Lewis, J. Schieber, N. Mangold, R. Milliken, P. G. Conrad, D. D. Marais, J. Farmer, K. Siebach, F. Calef III, J. Hurowitz, S. M. M. Lennan, D. Ming, D. Vaniman, J. Crisp, A. Vasavada, K. S. Edgett, M. Malin, D. Blake, R. Gellert, P. Mahaffy, R. C. Wiens, S. Maurice, J. A. Grant, S. Wilson, R. C. Anderson, L. Beegle, R. Arvidson, B. Hallet, R. S. Sletten, M. Rice, J. Bell III, J. Griffes, B. Ehlmann, R. B. Anderson, T. F. Bristow, W. E. Dietrich, G. Dromart, J. Eigenbrode, A. Fraeman, C. Hardgrove, K. Herkenhoff, L. Jandura, G. Kocurek, S. Lee, L. A. Leshin, R. Leveille, D. Limonadi, J. Maki, S. M. Closkey, M. Meyer, M. Minitti, H. Newsom, D. Oehler, A. Okon, M. Palucis, T. Parker, S. Rowland, M. Schmidt, S. Squyres, A. Steele, E. Stolper, R. Summons, A. Treiman, R. Williams, A. Yingst, MSL Science Team, A habitable fluvio-lacustrine environment at Yellowknife Bay, Gale Crater Mars. *Science* **343**, 12427777 (2013).
4. Y. Ohtomo, T. Kakegawa, A. Ishida, T. Nagase, M. T. Rosing, Evidence for biogenic graphite in early Archaean Isua metasedimentary rocks. *Nat. Geosci.* **7**, 25–28 (2014).
5. P. J. Boston, Location, location, location! Lava caves on Mars for habitat, resources, and the search for life. *J. Cosmol.* **12**, 3957–3979 (2010).
6. J. C. Spagna, A. M. Peattie, Terrestrial locomotion in arachnids. *J. Insect Physiol.* **58**, 599–606 (2012).
7. J. M. Fernandez, Advanced deployable shell-based composite booms for small satellite structural applications including solar sails, paper presented at 4th International Symposium on Solar Sailing, Tokyo, Japan, 17 to 20 January 2017.
8. J. Footdale, T. Murphey, Mechanism design and testing of a self-deploying structure using flexible composite tape springs, in *Proceedings of the 42nd Aerospace Mechanisms Symposium* (NASA, 2014), pp. 497–510.
9. B. R. Spence, S. White, M. LaPointe, S. Kiefer, P. LaCorte, J. Banik, D. Chapman, J. Merrill, International Space Station (ISS) Roll-Out Solar Array (ROSA) spaceflight experiment mission and results, in *2018 IEEE 7th World Conference on Photovoltaic Energy Conversion* (IEEE, 2018), pp. 3522–3529.
10. D. Baioni, M. Sgavetti, Karst terrains as possible lithologic and stratigraphic markers in northern Sinus Meridiani, Mars. *Planet. Space Sci.* **75**, 173–181 (2013).
11. S. Schneider, A. Bylard, T. G. Chen, P. Wang, M. R. Cutkosky, M. Pavone, ReachBot: A small robot for large mobile manipulation tasks, in *2022 IEEE Aerospace Conference* (IEEE, 2022), pp. 1–12.
12. T. G. Chen, B. Miller, C. Winston, S. Schneider, A. Bylard, M. Pavone, M. R. Cutkosky, ReachBot: A small robot with exceptional reach for rough terrain, in *2022 International Conference Robotics and Automation* (IEEE, 2022), pp. 4517–4523.
13. S. Newdick, T. G. Chen, B. Hockman, E. Schmerling, M. R. Cutkosky, M. Pavone, Designing reachbot: System design process with a case study of a martian lava tube mission, in *2023 IEEE Aerospace Conference* (IEEE, 2023), pp. 1–9.
14. S. Newdick, N. Ongole, T. G. Chen, E. Schmerling, M. Cutkosky, M. Pavone, Motion planning for a climbing robot with stochastic grasps, in *2023 IEEE International Conference on Robotics and Automation* (IEEE, 2023), pp. 11838–11844.
15. A. Bicchi, V. Kumar, Robotic grasping and contact: A review, in *Proceedings 2000 ICRA Millennium Conference IEEE International Conference on Robotics and Automation Symposia Proceedings* (IEEE, 2000), pp. 348–353.
16. L. Han, J. C. Trinkle, Z. X. Li, Grasp analysis as linear matrix inequality problems. *IEEE Trans. Robot. Autom.* **16**, 663–674 (2000).
17. Z. Li, P. Hsu, S. Sastry, Grasping and coordinated manipulation by a multifingered robot hand. *Int. J. Robot. Res.* **8**, 33–50 (1989).
18. K. Nagai, T. Yoshikawa, Dynamic manipulation/grasping control of multifingered robot hands. *Trans. Soc. Instrum. Control Eng.* **30**, 39–47 (1994).
19. S. Kuindersma, R. Deits, M. Fallon, A. Valenzuela, H. Dai, F. Permenter, T. Koolen, P. Marion, R. Tedrake, Optimization-based locomotion planning, estimation, and control design for the Atlas humanoid robot. *Autom. Robot.* **40**, 429–455 (2016).
20. K. Hauser, T. Bretl, J.-C. Latombe, Non-gaited humanoid locomotion planning, in *IEEE RAS International Conference on Humanoid Robots* (IEEE, 2005), pp. 7–12.
21. T. Bretl, Motion planning of multi-limbed robots subject to equilibrium constraints: The free-climbing robot problem. *Int. J. Robot. Res.* **25**, 317–342 (2006).
22. A. Parness, N. Abcouwer, C. Fuller, N. Wiltsie, J. Nash, B. Kennedy, Lemur 3: A limbed climbing robot for extreme terrain mobility in space, in *2017 IEEE International Conference on Robotics and Automation (ICRA)* (IEEE, 2017), pp. 5467–5473.
23. J. Nakanishi, T. Fukuda, D. E. Koditschek, A brachiating robot controller. *IEEE Trans. Robot. Autom.* **16**, 109–123 (2000).
24. A. Parness, Testing gecko-like adhesives aboard the International Space Station, in *AIAA SPACE and Astronautics Forum & Exposition* (ARC, 2017).
25. R. Zhang, J.-C. Latombe, Capuchin: A free-climbing robot. *Int. J. Adv. Robot. Syst.* **10**, (2013).
26. J. Lamaury, M. Gouttefarde, M. Michelin, O. Tempier, Design and control of a redundant suspended cable-driven parallel robots, in *Latest Advances in Robot Kinematics* (Springer, 2012), pp. 237–244.
27. A. Capua, A. Shapiro, S. Shoval, Spiderbot: A cable-suspended walking robot. *Mech. Mach. Theory.* **82**, 56–70 (2014).
28. S. Qian, B. Zi, W.-W. Shang, Q.-S. Xu, A review on cable-driven parallel robots. *Chin. J. Mech. Eng.* **31**, 66 (2018).
29. S. Seriani, P. Gallina, A. Wedler, A modular cable robot for inspection and light manipulation on celestial bodies. *Acta Astronaut.* **123**, 145–153 (2016).
30. P. McGarey, D. Yoon, T. Tang, F. Pomerleau, T. D. Barfoot, Developing and deploying a tethered robot to map extremely steep terrain. *J. Field Robot.* **35**, 1327–1341 (2018).
31. I. A. Nesnas, J. B. Matthews, P. Abad-Manterola, J. W. Burdick, J. A. Edlund, J. C. Morrison, R. D. Peters, M. M. Tanner, R. N. Miyake, B. S. Solish, R. C. Anderson, Axel and duaxel rovers for the sustainable exploration of extreme terrains. *J. Field Robot.* **29**, 663–685 (2012).
32. A. T. Asbeck, S. Kim, M. R. Cutkosky, W. R. Provancher, M. Lanzetta, Scaling hard vertical surfaces with compliant microspine arrays. *Int. J. Robot. Res.* **25**, 1165–1179 (2006).
33. S. Wang, H. Jiang, T. Myung Huh, D. Sun, W. Ruotolo, M. Miller, W. R. Roderick, H. S. Stuart, M. R. Cutkosky, Spinyhand: Contact load sharing for a human-scale climbing robot. *J. Mech. Robot.* **11**, 031009 (2019).
34. P. Zi, K. Xu, Y. Tian, X. Ding, A mechanical adhesive gripper inspired by beetle claw for a rock climbing robot. *Mech. Mach. Theory* **181**, 105168 (2023).
35. A. Parness, M. Frost, N. Thatte, J. P. King, K. Witkoe, M. Nevarez, M. Garrett, H. Aghazarian, B. Kennedy, Gravity-independent rock-climbing robot and a sample acquisition tool with microspine grippers. *J. Field Robot.* **30**, 897–915 (2013).
36. S. B. Backus, R. Onishi, A. Bocklund, A. Berg, E. D. Contreras, A. Parness, Design and testing of the jpl-nautilus gripper for deep-ocean geological sampling. *J. Field Robot.* **37**, 972–986 (2020).
37. A. Parness, A. Willig, A. Berg, M. Shekels, V. Arutyunov, C. Dandino, B. Kennedy, A microspine tool: Grabbing and anchoring to boulders on the Asteroid Redirect Mission, in *2017 IEEE Aerospace Conference* (IEEE, 2017), pp. 1–10.
38. A. T. Asbeck, M. R. Cutkosky, Designing compliant spine mechanisms for climbing. *J. Mechanisms Robotics* **4**, 031007 (2012).
39. H. Jiang, S. Wang, M. R. Cutkosky, Stochastic models of compliant spine arrays for rough surface grasping. *Intl. J. Robot. Res.* **37**, 669–687 (2018).
40. S. Iacoponi, M. Calisti, C. Laschi, Simulation and analysis of microspines interlocking behavior on rocky surfaces: An in-depth study of the isolated spine. *J. Mech. Robot.* **12**, 061016 (2020).
41. M. Zucker, J. A. Bagnell, C. G. Atkeson, J. Kuffner, An optimization approach to rough terrain locomotion, in *2010 IEEE International Conference on Robotics and Automation* (IEEE, 2010), pp. 3589–3595.
42. P. D. Neuhaus, J. E. Pratt, M. J. Johnson, Comprehensive summary of the institute for human and machine cognition's experience with littledog. *Intl. J. Robot. Res.* **30**, 216–235 (2011).
43. J. Z. Kolter, Y. Kim, A. Y. Ng, Stereo vision and terrain modeling for quadruped robots, in *2009 IEEE International Conference on Robotics and Automation* (IEEE, 2009), pp. 1557–1564.
44. M. Tranzatto, T. Miki, M. Dharmadhikari, L. Bernreiter, M. Kulkarni, F. Mascarich, O. Andersson, S. Khattak, M. Hutter, R. Siegwart, K. Alexis, CERBERUS in the DARPA subterranean challenge. *Sci. Robot.* **7**, eabp9742 (2022).

45. R. M. Murray, Z. Li, S. S. Sastry, *A Mathematical Introduction to Robotic Manipulation* (CRC Press, ed. 1, 1994).
46. S. Wang, H. Jiang, M. R. Cutkosky, Design and modeling of linearly-constrained compliant spines for human-scale locomotion on rocky surfaces. *Intl. J. Robot. Res.* **36**, 985–999 (2017).
47. W. Ruotolo, F. S. Roig, M. R. Cutkosky, Load-sharing in soft and spiny paws for a large climbing robot. *IEEE Robot. Autom. Lett.* **4**, 1439–1446 (2019).
48. W. R. Roderick, H. Jiang, S. Wang, D. Lentink, M. R. Cutkosky, Bioinspired grippers for natural curved surface perching, in *Biomimetic and Biohybrid Systems: 6th International Conference, Living Machines 2017*, M. Mangan, M. Cutkosky, A. Mura, P. Verschure, T. Prescott, N. Lepora, Eds., vol. 10384 of Lecture Notes in Computer Science (Springer, 2017), pp. 604–610.
49. M. G. Catalano, G. Grioli, E. Farnioli, A. Serio, C. Piazza, A. Bicchi, Adaptive synergies for the design and control of the Pisa/IIT SoftHand. *Intl. J. Robot. Res.* **33**, 768–782 (2014).
50. M. Baril, T. Laliberté, F. O. Guay, C. M. Gosselin, Static analysis of single-input/multiple-output tendon-driven underactuated mechanisms for robotic hands, in *International Design Engineering Technical Conferences and Computers and Information in Engineering Conference* (ASME, 2010), pp. 155–164.
51. B. Belzile, L. Birglen, Stiffness analysis of double tendon underactuated fingers, in *2014 IEEE International Conference on Robotics and Automation (ICRA)* (IEEE, 2014), pp. 6679–e6684.
52. H. Stuart, S. Wang, O. Khatib, M. R. Cutkosky, The ocean one hands: An adaptive design for robust marine manipulation. *Intl. J. Robot. Res.* **36**, 150–166 (2017).
53. L. Gerez, G. Gao, M. Liarokapis, Employing magnets to improve the force exertion capabilities of adaptive robot hands in precision grasps, in *2019 IEEE/RSJ International Conference on Intelligent Robots and Systems (IROS)* (IEEE, 2019), pp. 7630–7635.
54. A. Gafer, D. Heymans, D. Prattichizzo, G. Salvietti, The quad-spatula gripper: A novel softrigid gripper for food handling, in *2020 3rd IEEE International Conference on Soft Robotics (RoboSoft)* (IEEE, 2020), pp. 39–45.
55. M. A. Fischler, R. C. Bolles, Random sample consensus: A paradigm for model fitting with applications to image analysis and automated cartography. *Comm. ACM* **24**, 381–395 (1981).
56. R. Schnabel, R. Wahl, R. Klein, Efficient RANSAC for point-cloud shape detection. *Comput. Graph. Forum* **26**, 214–226 (2007).
57. P. H. Torr, A. Zisserman, Robust parameterization and computation of the trifocal tensor. *Image Vis. Comput.* **15**, 591–605 (1997).
58. P. H. Torr, A. Zisserman, Mlesac: A new robust estimator with application to estimating image geometry. *Comput. Vis. Image Underst.* **78**, 138–156 (2000).
59. J. G. Blank, T. L. Roush, C. L. Stoker, A. Colaprete, S. Datta, U. Wong, J. Wynne, Planetary caves as astrobiology targets, in *AGU Fall Meeting Abstracts* (AGU, 2018), pp. P21H-3428.
60. T. N. Titus, J. J. Wynne, M. J. Malaska, A.-A. Agha-Mohammadi, P. B. Buhler, E. C. Alexander, J. W. Ashley, A. Azua-Bustos, P. J. Boston, D. L. Buczkowski, L. Chiao, G. E. Cushing, J. De Decker, P. de León, C. Demirel-Floyd, J. De Waele, A. G. Fairén, A. Frumkin, G. L. Harris, H. Jones, L. H. Kerber, E. J. Leonard, R. J. Léveillé, K. Manyapu, M. Massironi, A. Z. Miller, J. E. Mylroie, B. P. Onac, S. Parazynski, C. B. Phillips, C. M. Phillips-Lander, T. H. Prettyman, H. M. Sapers, F. Sauro, N. Schorghofer, D. Schulze-Makuch, J. E. Scully, K. Uckert, R. V. Wagner, W. L. Whittaker, K. E. Williams, U. Y. Wong, A roadmap for planetary caves science and exploration. *Nat. Astron.* **5**, 524–525 (2021).
61. J. J. Wynne, J. E. Mylroie, T. N. Titus, M. J. Malaska, D. L. Buczkowski, P. B. Buhler, P. K. Byrne, G. E. Cushing, A. G. Davies, A. Frumkin, C. Hansen-Koharcheck, V. Hiatt, J. D. Hofgartner, T. Hoogenboom, U. Horodyskyj, K. Hughson, L. Kerber, M. Landis, E. J. Leonard, E. Lesage, A. Lucchetti, M. Massironi, K. L. Mitchell, L. Penasa, C. B. Phillips, R. Pozzobon, J. Radebaugh, F. Sauro, R. V. Wagner, T. R. Watter, Planetary caves: A solar system view of processes and products. *J. Geophys. Res. Planets* **127**, e2022JE007303 (2022).
62. J. J. Wynne, T. N. Titus, A. Agha-Mohammadi, A. Azua-Bustos, P. J. Boston, P. de León, C. Demirel-Floyd, J. De Waele, H. Jones, M. J. Malaska, A. Z. Miller, H. M. Sapers, F. Sauro, D. L. Sonderegger, K. Uckert, U. Y. Wong, E. Calvin Alexander Jr., L. Chiao, G. E. Cushing, J. De Decker, A. G. Fairén, A. Frumkin, G. L. Harris, M. L. Kearney, L. Kerber, R. J. Léveillé, K. Manyapu, M. Massironi, J. E. Mylroie, B. P. Onac, S. E. Parazynski, C. M. Phillips-Lander, T. H. Prettyman, D. Schulze-Makuch, R. V. Wagner, W. L. Whittaker, K. E. Williams, Fundamental science and engineering questions in planetary cave exploration. *J. Geophys. Res. Planets* **127**, e2022JE007194 (2022).
63. C. M. Phillips-Lander, A. Agha-mohamamdi, J. J. Wynne, T. N. Titus, N. Chanover, C. Demirel-Floyd, K. Uckert, K. E. Williams, D. Wyrick, J. Blank, P. J. Boston, K. Mitchell, A. Kereszturi, J. Martin-Torres, S. Shkolyar, N. Bardabelias, S. Datta, K. Retherford, L. Sam, A. Bahardwaj, A. Fairén, D. Flannery, R. C. Wiens, Mars astrobiological cave and internal habitability explorer (MACIE): A new frontiers mission concept. *Bull. Am. Astron. Society* **53**, (2021).
64. F. M. Phillips, Cosmogenic ^{36}Cl ages of quaternary basalt flows in the Mojave Desert, California, USA. *Geomorphology* **53**, 199–208 (2003).
65. W. Wise, Geologic map of the Pisgah and Sunshine cone lava fields, California. NASA Tech. Lett. 11 (1966).
66. R. Greeley, N. Lancaster, R. J. Sullivan, R. S. Saunders, E. Theilig, S. Wall, A. Dobrovolskis, B. R. White, J. D. Iversen, A relationship between radar backscatter and aerodynamic roughness: Preliminary results. *Geophys. Res. Lett.* **15**, 565–568 (1988).
67. R. E. Arvidson, C. Acton, D. Blaney, J. Bowman, S. Kim, G. Klingelhöfer, J. Marshall, C. Niebur, J. Plescia, R. S. Saunders, C. T. Ulmer, Rocky 7 prototype Mars rover field geology experiments: 1. lavic lake and sunshine volcanic field, california. *J. Geophys. Res. Planets* **103**, 22671–22688 (1998).

Acknowledgments: We thank Stanford University and the Stanford Research Computing Center for providing computational resources and support that contributed to these research results (Sherlock cluster). **Funding:** This work was supported by the NASA Innovative Advanced Concepts (NIAC) program. S.N. and J.D. are supported by NASA Space Technology Graduate Research Opportunities (NSTGRO). **Author contributions:** The gripper was designed by T.G.C. The gripper modeling was constructed by T.G.C., J.D., and C.B. The simulation and motion planning was conducted by S.N. The reachability analysis was performed by N.O. The grasp site detection was conducted by J.D. The field testing was conducted by T.G.C., J.D., and S.N. The supervision of the project was provided by M.L., M.P., and M.R.C. **Data and materials availability:** All data needed to evaluate the conclusions in the paper are present in the paper or the Supplementary Materials. Data and code can be found here: 10.5281/zenodo.10836305.

Submitted 31 May 2023
Accepted 19 March 2024
Published 17 April 2024
10.1126/scirobotics.adi9762

Science Robotics

Locomotion as manipulation with ReachBot

Tony G. Chen, Stephanie Newdick, Julia Di, Carlo Bosio, Nitin Ongole, Mathieu Lapôtre, Marco Pavone, and Mark R. Cutkosky

Sci. Robot. **9** (89), eadi9762. DOI: 10.1126/scirobotics.adi9762

Editor's summary
Caves on the moon and Mars are of geological and astrobiological interest, but their rocky terrain and sparse anchor points make it impossible for traditional robots to explore. Taking inspiration from an arachnid, Chen *et al*. developed a robot with a small body and long extendable booms for appendages named ReachBot. The ends of the booms were equipped with grippers that can grasp rocky terrain and enable ReachBot to use manipulation for locomotion. Using onboard sensors along with a contact-before-motion planner, the robot could scan and identify graspable convex features. Field tests performed in a lava tube in the Mojave Desert (California, USA) confirmed that ReachBot could identify and grasp multiple sites, demonstrating its potential as a martian explorer. —Melisa Yashinski